Efficient ceramic anodes infiltrated with binary and ternary electrocatalysts for SOFCs operating at low temperatures

A. Mohammed Hussain*, Jens V.T. Høgh, Wei Zhang, Nikolaos Bonanos

DTU Energy Conversion (formerly known as 'Risø National Laboratory for Sustainable Energy'), Department of Energy Conversion and Storage, Risø Campus, Technical University of Denmark, Roskilde 4000, Denmark

HIGHLIGHTS

► Infiltration of Ni, Pt, Pd, Ru and CGO electrocatalysts precursors.
► Strontium titanate based ceramic anodes with an addition of Ni in noble metals containing electrocatalysts.
► Binary and ternary electrocatalyst for hydrogen oxidation.
► Low temperature solid oxide fuel cells.

ARTICLE INFO

ABSTRACT

Electrocatalyst precursor of various combinations: Pt, Ru, Pd, Ni and Gd-doped CeO_2 (CGO) were infiltrated into a porous $Sr_{0.94}Ti_{0.9}Nb_{0.1}O_3$ (STN) backbone, to study the electrode performance of infiltrated ceramic anodes at low temperature ranges of 400–600 °C. The performance of the binary electrocatalyst infiltrated ceramic backbones are Pt–CGO>Ru–CGO>Pd–CGO>Ni–CGO. Ternary electrocatalyst of Ni–Pd–CGO and Ni–Pt–CGO showed the lowest polarization resistance of 0.31 and 0.11 Ωcm^2, respectively at 600 °C in H_2/3% H_2O. The average particle size of the ternary electrocatalyst was larger than the binary Pd–CGO and Pt–CGO due to the particle coarsening of Ni nanoparticles. High resolution transmission electron microscopic analysis on the best performing Ni–Pt–CGO electrocatalyst infiltrated anode reveals the formation of Ni–Pt nanocrystalline alloy and a homogenous distribution of nanoparticles on STN backbone.

© 2012 Elsevier B.V. All rights reserved.

1. Introduction

Highly efficient electrodes and thin electrolytes are considered as major requirements for production of efficient power from low temperature SOFCs (LT-SOFCs) [1,2]. In particular to anodes, the most commonly studied for LT-SOFCs are based on cermet of nickel and an oxide ion conductor, e.g. Ni–CGO (Gd-doped ceria) [3]. Many recent studies on cermet anodes have been focused on controlling the parameters such as grain size, porosity, Ni and CGO ratio, stoichiometry of CGO etc., However, the polarization resistances remains relatively high at 400 °C in moisturized H_2 fuel [3–5]. The poor redox stability of Ni and intolerance to

hydrocarbon fuels indicates the need for the development of alternative anode materials for LT-SOFCs [6,7].

Perovskite type ceramic oxides have recently been considered as promising alternative anode materials for LT-SOFCs. $SrTiO_3$ perovskite oxide has tolerance to sulfur and carbon poisoning and is considered as potential anodes for SOFCs operable in hydrocarbon fuels [8,9]. In particular, donor-doped $SrTiO_3$ perovskite e.g., Nb-doped $SrTiO_3$ attracted the anode development researchers of SOFC [10]. This material exhibits metallic type electronic conductivity and good redox stability. Two known major drawbacks of using this material as SOFC anodes are poor electrocatalysts activity for H_2 oxidation and low oxide ion conductivity. The incorporation of nanostructured electrocatalyst into an STN backbone (porous skeletal structure) makes it a potential candidate for LT-SOFC anodes. The electrocatalytic activity for hydrogen oxidation and oxide ion conductivity can be achieved by modifying the perovskite oxide with CeO_2 or by infiltrations [11,12].

* Corresponding author. Tel.: +45 46775639; fax: +45 46775858.
 E-mail addresses: abhu@risoe.dtu.dk, uzzain@gmail.com (A.M. Hussain).

Nanostructured, oxide ion conducting materials based on CeO_2 doped with other rare earth elements (Gd, Sm and Y) are widely recognized as mixed ionic and electronic conductors in reducing gas conditions. In addition, these materials have catalytic properties for hydrogen oxidation [13]. A few percent (1–2 wt. %) of metallic catalyst such as Ni mixed with Gd-doped ceria (CGO) infiltrated in $Sr_{0.94}Ti_{0.9}Nb_{0.1}O_3$ (STN) backbone enhanced the SOFC anode performance considerably compared to CGO alone [12,14]. A careful control on loading of electrocatalyst in STN helps in tuning the performance. Results reported in literature prompts to explore other catalytic metals for hydrogen oxidation in combination with Ni [15–17]. Infiltration technology significantly contributes to reducing the quantity of noble metals needed to obtain beneficial electrochemical properties and allows the exploration of nanostructured, noble metal-ceramic catalysts in combinations [17]. Although Ni–CGO infiltrated STN has shown reasonably good anode performance, further improvements for LT-SOFC anodes can be made by employing a small quantity of noble metals e.g. Pt, Ru, Pd etc., in combination with Ni.

This work concentrates on electrochemical characterization of STN anodes infiltrated with binary electrocatalysts Pt–CGO, Ru–CGO, Pd–CGO, and Ni–CGO operating at low temperature (<600 °C). Pt–CGO showed the best performance in comparison to all other binary electrocatalyst. Among the ternary electrocatalysts being investigated, Ni–Pt–CGO infiltrated STN anodes showed an excellent performance. Emphasis was given to understand the nanocrystalline properties of Ni–Pt in the Ni–Pt–CGO using high-resolution transmission electron microscopy. It is observed that the lattice parameter of Ni–Pt alloy is located in between the two individual metals (i.e., Ni and Pt). The observed alloying of the metallic catalyst and nanostructured morphology of the electrocatalyst are believed to be the reason for an improved anode performance.

2. Experimental section

2.1. STN synthesis

STN perovskite oxide was prepared using a wet chemical synthesis route. Strontium carbonate ($SrCO_3$), titanium (IV) iso-propoxide (Ti $\{OCH(CH_3)_2\}_4$) and niobium oxalate (C_2NbO_4) were used as starting materials (Sigma Aldrich) to obtain an STN composition of $Sr_{0.94}Ti_{0.9}Nb_{0.1}O_3$. A 260 ml of titanium (IV) iso-propoxide and 160 ml of niobium oxalate was mixed separately in an already prepared 500 ml ethanol and water mixture in a proportion of 1:1.5. The resulted precipitates were filtered, washed in ethanol and dried. Subsequently, the hydroxides were dissolved separately in citric acid monohydrate (HOC(COOH)(CH$_2$-COOH)$_2$·H$_2$O) with the addition of 20 ml hydrogen peroxide (H_2O_2) solution. The concentration of Nb and Ti containing solutions was 5.7 and 2.1 wt. %. About 13.9 g of $SrCO_3$ powder along with 20 ml of H_2O_2 was added slowly into 125.5 g of Ti and 63 g of Nb ion containing solutions. This mixture was placed in a crucible and heated on a hot plate at 300 °C for 5 h. The resulting solids were heat-treated at 1000 °C for 3 h and ground to fine powder. The crystalline peaks of STN were confirmed using XRD for each batch.

2.2. Symmetrical cell preparation for the characterization of anode

STN powder was formulated as a screen printing ink following an in-house preparation procedure using surfactant, plasticizer and a binder and mixed thoroughly by using a mechanical shaker overnight. The screen printed STN on a dense ScYSZ (10 mol % Sc_2O_3, 1 mol % Y_2O_3 stabilized ZrO_2) tapes of 120 μm thick were sintered for 4 h in a reducing atmosphere (9% H_2/N_2). The porous STN anodes were deposited on both sides of the ScYSZ electrolyte with an area of 6×6 cm^2. The tape was cut into smaller pieces measuring an area of 0.25 cm^2 for use in the electrochemical setup.
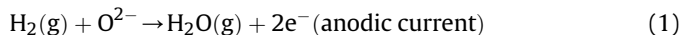
A 0.75 M of CGO precursor solution was prepared by dissolving cerium nitrate (Ce(NO$_3$)$_3$· 6H$_2$O) and gadolinium nitrate (Gd(NO$_3$)$_3$· 6H$_2$O) in H$_2$O along with polymer surfactants. The composition of the precursor was $Ce_{0.8}Gd_{0.2}O_{2-\delta}$. The precursor solution of Ni–CGO, Pt–CGO contains 25 wt. % of Ni and 25 wt. % of Pt, respectively relative to CGO and was prepared by dissolving 0.6 M nickel nitrate (Ni (NO$_3$)$_2$· 6H$_2$O) and 0.2 M of tetra ammine platinum (II) nitrate (H$_{12}$N$_6$O$_6$Pt) in already prepared CGO precursors.

For Pd-CGO, approximately 10 wt. % Pd in the form of palladium nitrate (Pd (NO$_3$)$_2$· 6H$_2$O) with a concentration of 0.6 M was dissolved in CGO precursors. In case of the Ru–CGO containing infiltrates, 25 wt. % of Ru in the form of ruthenium chloride (RuCl$_3$· xH$_2$O) with a concentration of 0.3 M was dissolved in CGO precursor. The infiltrated STN anodes were prepared by adding a few drops of the precursor into the symmetrical cells, after which they were placed in a vacuum chamber. Vacuum was applied in order to remove air bubbles from the porous STN backbone and to facilitate the liquid precursor to homogeneously coat the surface of the anode. For binary electrocatalyst (BEC) infiltration, Pt–CGO, Ru–CGO, Pd–CGO and Ni–CGO were infiltrated 3 times to increase the loadings in porous STN; after each infiltration the cells were calcined at 350 °C for 1 h. In case of ternary electrocatalyst (TEC) infiltration such as Ni–Pd–CGO and Ni–Pt–CGO, dual infiltrations were carried out. Firstly, Pd–CGO and Pt–CGO were infiltrated two times and followed by infiltration of Ni–CGO 3 times. The heat treatments were performed after each infiltration. The change in weight after calcinations was recorded after each infiltration. The EC samples for physico chemical and microscopic analysis were prepared under the similar conditions as that of electrocatalysts infiltrated in STN backbone.

2.3. Anode characterization

A Solartron SI1260 frequency response analyzer was used to measure the impedance of the symmetrical cells. The symmetrical cells were electrically contacted using Pt-paste (Ferro GmbH) and a Pt-grid. The polarization resistance of Pt paste as anode is very high (123 Ωcm^2 at 650 °C in H$_2$/3% H$_2$O) owing to their larger grain sizes and lack of oxide ion conductivity. The contribution from Pt current collector is negligible and the same current collector was used for all the anodes to compare the results [5,18]. The cells were heated to 650 °C in 9% H$_2$/N$_2$, where after the gas was changed to dry H$_2$ (EMF = −1.312 V vs. air @650 °C) and kept for 12 h. The impedance spectra were recorded by applying an amplitude of 50 mV (the output voltage of the Solartron varies from 5 to 50 mV depending on the temperature of measurement and the resulting cell impedance) in the frequency range of 1 MHz–1 mHz. The impedance was measured in the temperature range 650 to 350 °C. The partial pressure of oxygen, (pO$_2$) was measured using an oxygen sensor. The EMF values were −1.125, −1.131, −1.140 and −1.147 V vs. air and the corresponding pO$_2$ were 10^{-26}, 10^{-27}, 10^{-29}, and 10^{-31} atm at 650, 600, 550 and 500 °C, respectively. These values correspond very well with the intended gas composition of 3% H$_2$O/H$_2$. All the obtained impedance spectra were corrected for inductance in the range of 30–60 nH originating from the leads of electrochemical setup depending on the sample position. The impedance spectra were fitted with equivalent circuit model using the code ZSimpWin with complex non-linear least squares fitting (CNLS). During impedance measurements on symmetrical cells, one side of the electrode will function as anode, while the other side functions as cathode. The anode and cathode

side changes with the alternating current. Hence, the reactions under investigation when using symmetrical cells are the hydrogen oxidation and the reduction of steam as shown in reactions (1) and (2).

$$H_2(g) + O^{2-} \rightarrow H_2O(g) + 2e^- \text{ (anodic current)} \quad (1)$$

$$H_2O(g) + 2e^- \rightarrow H_2(g) + O^{2-} \text{ (cathodic current)} \quad (2)$$

The crystal structure of the sintered STN anodes on ScYSZ symmetrical cells were determined using XRD with a Bruker D8 Bragg-Brentano diffractometer with Cu Kα radiation and compared with as-sintered STN powders. The microstructures of the symmetric cells and the STN backbone were examined by scanning electron microscope (SEM). A JEM-3000F transmission electron microscope was used to characterize the microstructure and chemical compositions of the samples.

3. Results and discussions

Fig. 1 shows the XRD of the TECs, Ni−Pd−CGO and Ni−Pt−CGO and are compared to that of Ni−CGO and CGO. The formation of fluorite-like single phase of CGO is evident even at a low calcination temperature of 350 °C (1 h, in air). No reaction occurred between the metal and ceramic phase, in other words, metal exists as a separate dispersed phase in a CGO matrix. XRD pattern of both TECs showed (111) reflex of Ni; however Pt and Pd peaks are not identified. The poor detection of X-ray reflections of such catalysts was already reported and is ascribed to its highly dispersed nature [19]. Moreover, a shift toward lower angle in Ni (111) is observed in Ni−Pt−CGO indicating a possible alloying.

The low thermal treatment of electrocatalysts at 650 °C in reducing atmosphere resulted in the nanostructured crystalline phase. The high resolution-transmission electron microscopy (HR-TEM) analysis was performed for the best performing Ni−Pt−CGO and is shown in Fig. 2. Both CGO and metallic phases were identified. The perpendicular (111) and (2−20) crystal planes of CGO are located at the right side of the figure; two small metallic grains are located on the left. The EDX quantification (Fig. S1 in the supporting information) reveals the average weight percent of Ni/Pt is in the ratio of 95:100 from 15 regions, consistent with the nominal ratio. Furthermore, a close observation on Fig. 2 illustrates that the lattice parameter of the alloy phase is situated in between those of Ni and Pt, indicating the formation of Ni−Pt alloy phase besides the CGO phase. However a small variation in lattice parameter at different area of measurements is envisaged, which are ascribed to coexistence of Ni and Pt elements in the Pt-Ni alloy phase. The Pt-Ni alloy
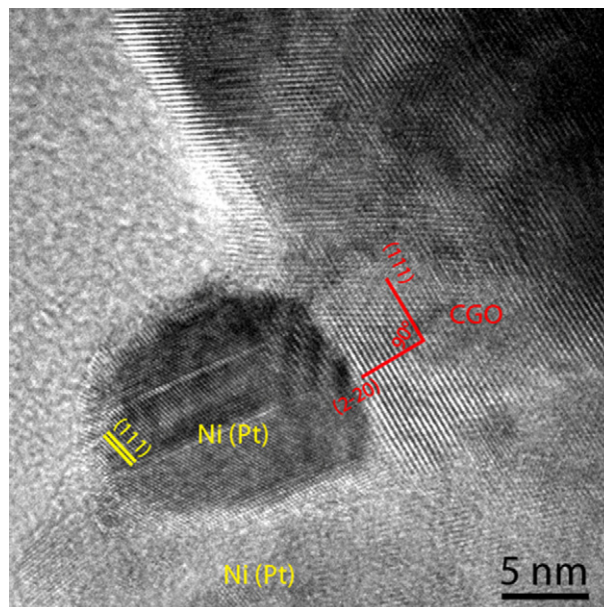

Fig. 2. HR-TEM image of Pt−Ni−CGO electrocatalyst. Heat treated at 650 °C in reducing atmosphere for 12 h.

phase adopts the same face-centered-cubic (FCC) structure as Pt and Ni phase, which are in good agreement with the XRD data. Additionally, in contrast to the pure Ni phase, some resultant lattice expansion was observed, e.g., the inter planar spacing of (111) plane is 2.3% larger than that of Ni. The resulted particle size of the infiltrated electrocatalysts were found to be around 5−10 nm and are highly dispersed.

The backbone for infiltration used in this study is Nb-doped, Sr deficient $SrTiO_3$ cubic perovskite with a composition of $Sr_{0.94}Ti_{0.9}Nb_{0.1}O_3$ prepared using a wet chemical method (see the Experimental Section for details). The powder XRD pattern of STN with a heat treatment at 1000 °C for 4 h (Fig. S2a in the supporting information) shows a single perovskite phase without formation of any secondary phases. The anodes were characterized using a symmetrical cell configuration of STN−ScYSZ−STN (XRD pattern of this symmetrical cell is shown in Fig. S2b of supporting information). The XRD pattern resembles as that of STN powder and few minor secondary phases were also detected. Formation of reduced TiO_2 (rutile) is expected for an STN sintered in reducing atmosphere [10,20]. However, the intensity of those unidentified peaks was very small. ScYSZ electrolyte peaks were seen along with STN peaks. The signal from the electrolyte was presumably detected through the porous electrode or could be from the sides of the symmetrical cell, where the electrolyte was exposed.

The scanning electron microscopy (SEM) micrographs of the BEC and TEC infiltrated STN anodes are shown in Fig. 3. The micrograph of BECs and TECs infiltrated STN anodes shows a uniform distribution of nanostructured CGO. It has also formed a percolated network in the STN backbone, which facilitates oxide ion conduction throughout the backbone. The nano-sized metal phase is found well dispersed in the CGO matrix and they are expected to act as active sites for hydrogen oxidation. For the Ni−Pd−CGO and Pt−Pd−CGO, the particle size of the metal phase is larger than Pd−CGO and Pt−CGO, respectively and is attributed to rapid particle growth of Ni nanoparticles than Pt and Pd nanoparticles.

Fig. 4a shows the impedance measurements of STN symmetrical cells infiltrated with Ni−CGO, Pd−CGO, Ru−CGO and Pt−CGO electroctalysts in H_2/3% H_2O at 600 °C. The obtained impedance spectra at 600 °C were fitted using the equivalent circuits, ($^1R_0$)
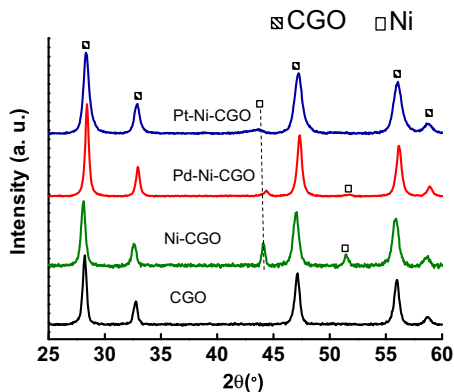

Fig. 1. XRD patterns of CGO, Ni−CGO, Pd−Ni−CGO and Pt−Ni−CGO electrocatalysts. The fluorite phase of CGO and Ni were labeled by a dashed line.
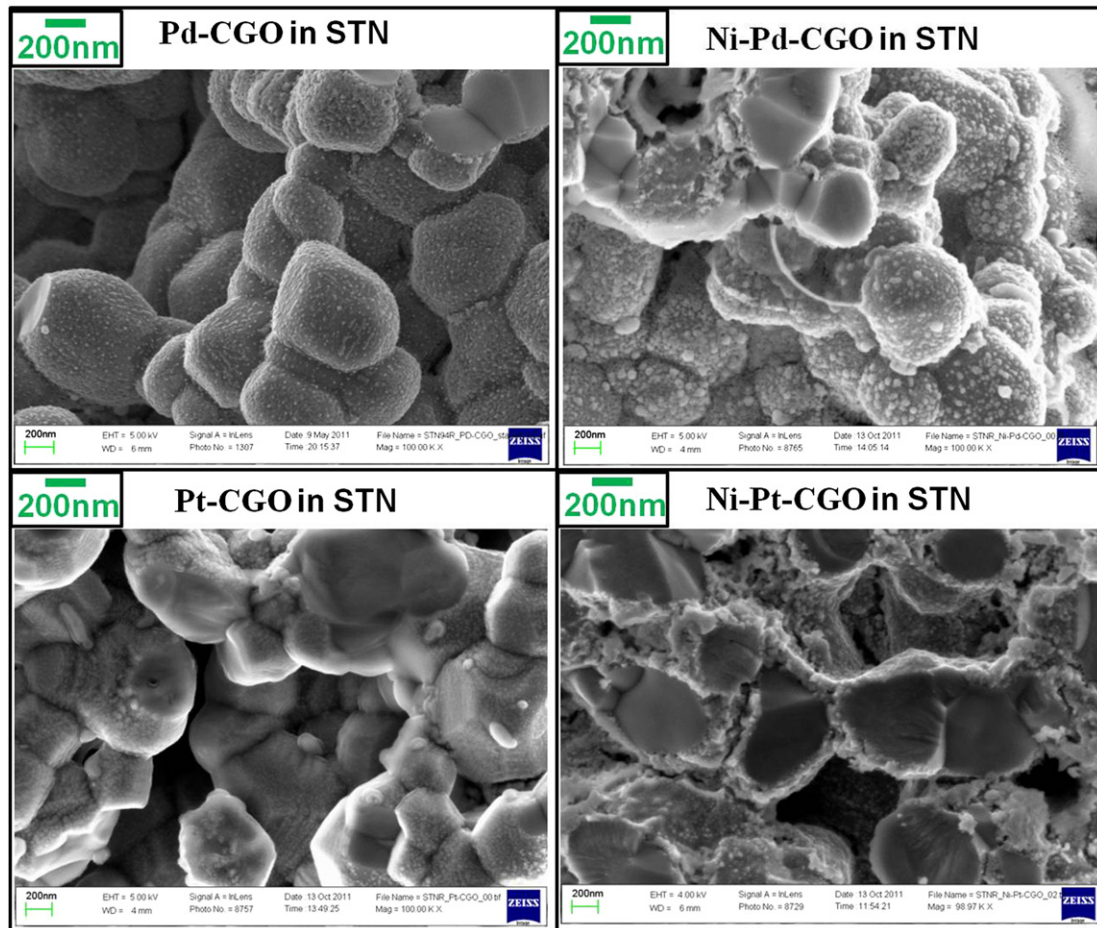
Fig. 3. SEM images (fractured cross section) of post-tested Pd–CGO, Ni–Pd–CGO, Pt–CGO and Ni–Pt–CGO infiltrated STN anodes.

(R_1Q_1), (R_2Q_2) and $(^1R_0)$ (R_0Q_0) (R_1Q_1) (R_2Q_2) with the number of sub-circuits depending on the number of impedance arcs obtained. The sum of $^1R_0$ and R_0 corresponds to the ohmic resistance of the electrolyte. R_1 and R_2 is the resistance due to the electrode processes. Q_1 and Q_2 correspond to the constant phase elements. R_0 was in the range of 1.5–1.9 Ωcm^2 at 600 °C for all the infiltrated anodes. The reason for this variation in ohmic resistance is discussed in the last section of this paper. The R_p (i.e. summation of R_1 and R_2) of the STN anode without infiltration shows a high value of 352 Ωcm^2; however it reduces to 0.96, 0.57, 0.51 and 0.16 Ωcm^2 for Ni–CGO, Pd–CGO, Ru–CGO and Pt–CGO, respectively at 600 °C. The drastic improvements in the electrode performance are due to the catalytic activity of the infiltrated Ni, Pd, Ru, Pt catalyst and CGO [16,21,22]. Although CGO exhibits catalytic activity, it cannot be used as a standalone electrocatalyst as such owing to its limited catalytic activity. The volume fractions of electrocatalyst infiltrated in the STN backbone were determined by measuring the change in weight after calcinations and is listed in Table 1.

Fig. 4b shows the Arrhenius plot of R_p. STN without infiltration has the highest slope in the Arrhenious plot. The activation energy (E_a) of STN is 1.14 eV. The slopes are slightly reduced with various infiltrates in STN backbone. The E_a of Ni–CGO, Pt–CGO, Ru–CGO and Pd–CGO in STN anodes were 1.09, 0.84, 0.93, and 0.97 eV, respectively. The values of E_a are almost the same for all the infiltrated STN anodes despite the lowering of R_p.

The electrochemical performances of Ni–CGO with addition of noble metal catalysts, such as Pd and Pt have been investigated using EIS. Fig. 5a shows the impedance spectra of STN infiltrated with
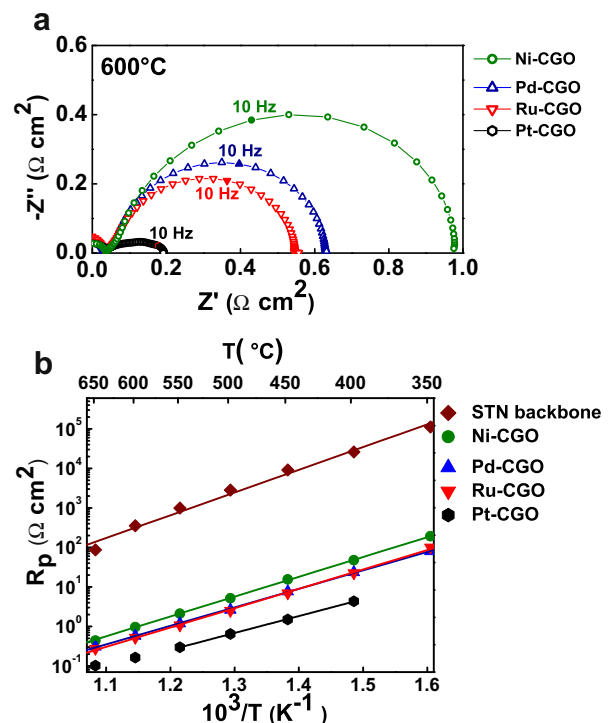

Fig. 4. a) Impedance spectra of Ni–CGO, Pd–CGO, Ru–CGO and Pt–CGO in 3% H$_2$O/H$_2$ at 600 °C and b) Arrhenius plot of electrode polarization resistance, R_p.

Table 1
Loading of electrocatalysts and the resulted polarization resistance (R_p) at 500 and 600 °C. The calculated activation energies of the anodes are listed.

Electrocatalysts	Loading (Vol. %)	R_P (Ωcm^2) at 600 °C	R_P (Ωcm^2) at 500 °C	Activation energy (eV)
Ni[1]–CGO	12.66	0.96	5.13	1.09
Pt[1]–CGO	7.63	0.16	0.64	0.84
Pd[1]–CGO	11.86	0.57	2.62	0.93
Ru[1]–CGO	18.09	0.51	2.5	0.97
Ni containing mixed catalysts				
Ni[1]–Pt[2]–CGO	13.20	0.1	0.3	0.85
Ni[1]–Pd[2]–CGO	14.26	0.31	1.62	0.98

Table 2
Resistances R_1, R_2 and R_3 and summit frequencies obtained from the equivalent circuit analysis of the impedance spectra at 600 °C in H_2/H_2O.

Electrocatalysts	$(R_1Q_1)_{HF}$		$(R_2Q_2)_{MF}$		$(R_3Q_3)_{LF}$		R_p (Ωcm^2)
	R_1 (Ωcm^2)	$F_{max, HF}$ (Hz)	R_2 (Ωcm^2)	$F_{max, HF}$ (Hz)	R_3 (Ωcm^2)	$F_{max, HF}$ (Hz)	
Pd–CGO	–	–	–	–	0.6	13	0.6
Ni–Pd–CGO	0.2	1940	0.2	144	0.015	9	0.41
Pt–CGO	0.09	2000	0.05	133	0.02	15	0.16
Ni–Pt–CGO	0.07	830	–	–	0.03	10	0.1

Ni–Pd–CGO and are compared with Pd–CGO. The values of R_p determined from impedance spectra of Ni–Pd–CGO infiltrated anodes is 0.31 Ωcm^2, while that of Pd–CGO is 0.57 Ωcm^2 at 600 °C. The parameters concerning the electrochemical characterization from the impedance spectra of Fig. 5a are listed Table 2. The value of R_p of Pd–CGO infiltrated anodes showed a single arc with a characteristics frequency of (13 Hz). Moreover, in this spectrum overlapping of electrode processes is observed and is difficult to interpret its physical meaning.

In the case of Ni-Pd-CGO infiltrated anodes, the impedance spectrum showed three distinct electrode processes, (R_1Q_1), (R_2Q_2) and (R_3Q_3) at high frequency (1 MHz-1000 Hz), middle frequency (1000–10 Hz) and low frequency (10–0.01 Hz), respectively. The R_1 at high frequency (HF) corresponds to interfacial resistance between the electrode/electrolyte [23], R_2 is resistance associated electrochemical hydrogen oxidation reaction at middle frequencies (MF) [16] and R_3 is due to the gas diffusion resistance at low frequency
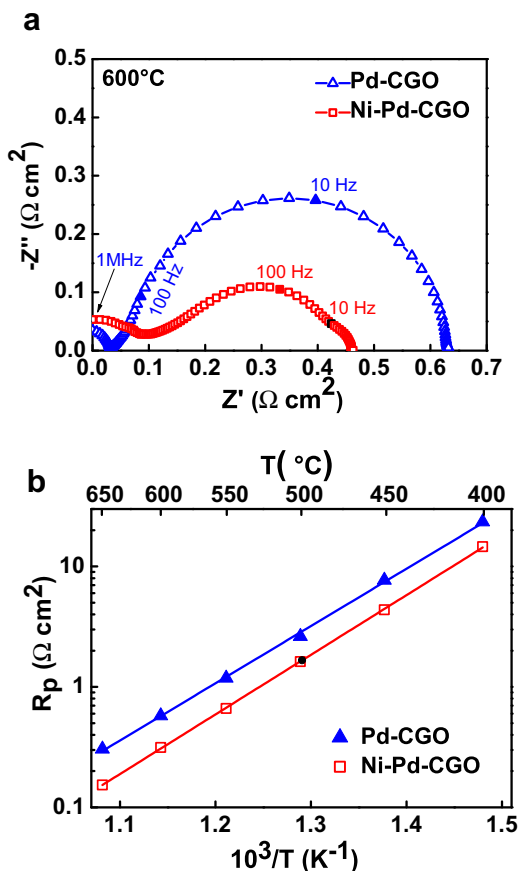
(LF). A small arc (R_0Q_0) originating at very high frequency of 1 MHz for the impedance spectra is associated with the bulk properties of the electrolyte and is confirmed by observing the impedance spectra measured at low temperatures. For each electrode process, the characteristic frequencies are listed in Table 2. The improvement in electrode performance can be ascribed to the synergistic electrocatalytic activty of Pd and Ni catalyst as reported in literature [16]. The activation energies of this electrocatalyst infiltrated anodes are calculated from the Arrhenius plot shown in Fig. 5b. E_a of Ni–Pd–CGO is 0.98 eV and this value is similar to Pd–CGO.

Similarly, the parameters concerning the electrochemical characterization of the Ni–Pt–CGO infiltrated anodes are listed in Table 2. The value of R_p of Ni–Pt–CGO electrocatalyst infiltrated anode is 0.1 Ωcm^2 determined from Fig. 6a. The value of R_p is lowest of the tested anodes and lower than Pt–CGO infiltrated anode, which is 0.16 Ωcm^2. For Pt–CGO infiltrated anodes R_1, R_2 and R_3 resistances associated with electrode processes described earlier were observed. The electrode resistance at HF associated with electrode electrolyte contact is lowered with Ni–Pt–CGO and MF arc associated with electrochemical hydrogen oxidation reaction resistance R_1 is completely disappeared. However, R_3 associated with gas diffusion at LF increased slightly. Most of the beneficial
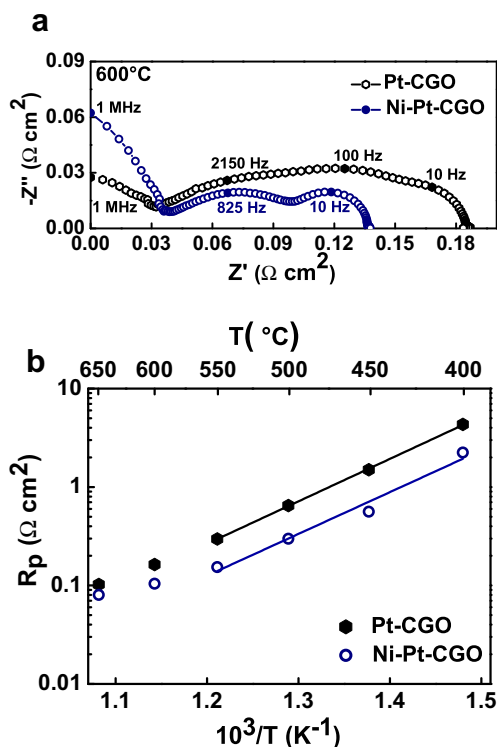

Fig. 5. a) Impedance spectra of Pd–CGO and Ni–Pd–CGO in 3% H_2O/H_2 at 600 °C and b) Arrhenius plot of electrode polarization resistance, R_p.

Fig. 6. a) Impedance spectra of Pt–CGO and Ni–Pt–CGO in 3% H_2O/H_2 at 600 °C and b) Arrhenius plot of electrode polarization resistance, R_p.

electrochemical properties are achieved from the Pt catalyst and nanocrystalline morphology of TEC. E_a of Ni–Pt–CGO anode is 0.85 eV as determined from the Arrhenius plot shown in Fig. 6b. E_a of Pt containing ternary and binary electrocatalyst are almost in the same range and has lower activation energy compared to other catalysts.

The same R_0 is expected among the anodes at one particular temperature e.g. 600 °C. This is a good indication in estimation of correct electrode polarization resistance (Fig. S3 in the supporting information shows the temperature dependence of R_0). The solid line indicates the R_0 of ScYSZ electrolyte for a thickness of 120 μm and was calculated based on the ionic conductivity reported in literature [24]. E_a obtained for ScYSZ electrolyte is 1.3 eV. The R_0 of the anodes infiltrated with various electrocatalyst are almost the same and have the same slope as that of theoretically calculated ScYSZ. However, the small variations in R_0 at high temperatures are probably due to the micro structural variations of the backbone and current collector contacts.

4. Conclusions

Nanostructured electrocatalyst suitable for low temperature solid oxide fuel cells anode were evaluated. Pt–CGO infiltrated STN anodes showed an electrode polarization resistance of 0.16 Ωcm^2, which is the lowest among the binary electrocatalysts. The addition of Ni in Pt–CGO and Pd–CGO by dual infiltrations further lowered the electrode polarization resistance. The morphology of the catalyst showed well dispersed metal nanoparticles distributed in the matrix of CGO. The nanocrystalline alloys of Ni–Pt were formed in Ni–Pt–CGO electrocatalyst along with the coexistence of Ni and Pt nanoparticles as separate phases.

Acknowledgment

Appendix A. Supporting information

Supporting information associated with this article can be found, in the online version, at doi:10.1016/j.jpowsour.2012.05.036.

References

[1] J. Huijsmans, F. Van Berkel, G. Christie, J. Power Sources 71 (1998) 107–110.
[2] X. Zhang, M. Robertson, S. Yick, C. Deces-Petit, E. Styles, W. Qu, Y. Xie, R. Hui, J. Roller, O. Kesler, J. Power Sources 160 (2006) 1211–1216.
[3] P. Kim, D. Brett, N. Brandon, J. Power Sources 189 (2009) 1060–1065.
[4] D.G. Ivey, E. Brightman, N. Brandon, J. Power Sources 195 (2010) 6301–6311.
[5] U.P. Muecke, K. Akiba, A. Infortuna, T. Salkus, N.V. Stus, L.J. Gauckler, Solid State Ionics 178 (2008) 1762–1768.
[6] P. Lohsoontorn, D. Brett, N. Brandon, J. Power Sources 175 (2008) 60–67.
[7] P. Lohsoontorn, D. Brett, N. Brandon, J. Power Sources 183 (2008) 232–239.
[8] P.R. Slater, D.P. Fagg, J.T.S. Irvine, J. Mater. Chem. 7 (1997) 2495–2498.
[9] M. Gong, X. Liu, J. Trembly, C. Johnson, J. Power Sources 168 (2007) 289–298.
[10] P. Blennow, K.K. Hansen, L. Wallenberg, M. Mogensen, J. Eur. Ceramic Soc. 27 (2007) 3609–3612.
[11] D.J. Cumming, J.A. Kilner, S. Skinner, J. Mater.Chem. 13 (2011) 5021–5026.
[12] S.P. Jiang, Int. J. Hydrogen Energy 37 (2011) 449–470.
[13] T. Sholklapper, C. Jacobson, S. Visco, L. De Jonghe, Fuel Cells 8 (2008) 303–312.
[14] A.M. Hussain, J.V.T. Høgh, T. Jacobsen, N. Bonanos, Int. J. Hydrogen Energy 37 (2012) 4309.
[15] H. Borchert, Y. Borchert, V.V. Kaichev, I.P. Prosvirin, G.M. Alikina, A.I. Lukashevich, V.I. Zaikovskii, E.M. Moroz, E.A. Paukshtis, V.I. Bukhtiyarov, J. Phys. Chem. B 109 (2005) 20077–20086.
[16] Y. Nabae, I. Yamanaka, M. Hatano, K. Otsuka, J. Electrochem. Soc. 153 (2006) A140.
[17] J.S. Kim, V.V. Nair, J.M. Vohs, R.J. Gorte, Scr. Mater. (2010).
[18] M. Guillodo, P. Vernoux, J. Fouletier, Solid State Ionics 127 (2000) 99–107.
[19] A. Tanksale, C. Zhou, J. Beltramini, G. Lu, J. Inclusion Phenomena Macrocyclic Chem. 65 (2009) 83–88.
[20] P. Blennow, A. Hagen, K.K. Hansen, L. Wallenberg, M. Mogensen, Solid State Ionics 179 (2008) 2047–2058.
[21] J. Rossmeisl, W.G. Bessler, Solid State Ionics 178 (2008) 1694–1700.
[22] T. Hibino, A. Hashimoto, M. Yano, M. Suzuki, M. Sano, Electrochim. Acta 48 (2003) 2531–2537.
[23] A. Babaei, S.P. Jiang, J. Li, J. Electrochem. Soc. 156 (2009) B1022–B1029.
[24] M. Laguna-Bercero, S. Skinner, J. Kilner, J. Power Sources 192 (2009) 126–131.